

# Piecewise Flat Embedding for Image Segmentation

Chaowei Fang, Zicheng Liao, Yizhou Yu

**Abstract**—We propose a new nonlinear embedding – Piecewise Flat Embedding (PFE) – for image segmentation. Based on the theory of sparse signal recovery, piecewise flat embedding attempts to recover a piecewise constant image representation with sparse region boundaries and sparse cluster value scattering. The resultant piecewise flat embedding exhibits interesting properties such as suppressing slowly varying signals, and offers an image representation with higher region identifiability which is desirable for image segmentation or high-level semantic analysis tasks. We formulate our embedding as a variant of the Laplacian Eigenmap embedding with an  $L_{1,p}$  ( $0 < p \leq 1$ ) regularization term to promote sparse solutions. First, we devise a two-stage numerical algorithm based on Bregman iterations to compute  $L_{1,1}$ -regularized piecewise flat embeddings. We further generalize this algorithm through iterative reweighting to solve the general  $L_{1,p}$ -regularized problem. To demonstrate its efficacy, we integrate PFE into two existing image segmentation frameworks, segmentation based on clustering and hierarchical segmentation based on contour detection. Experiments on four major benchmark datasets, *BSDS500*, *MSRC*, *Stanford Background Dataset*, and *PASCAL Context*, show that segmentation algorithms incorporating our embedding achieve significantly improved results.

**Index Terms**—Sparsity Models, Manifold Learning, Bregman Iterations, Image Segmentation.

## 1 INTRODUCTION

IMAGE segmentation decomposes an image into non-overlapping regions each of which covers pixels sharing common low-level (e.g. texture and color) or high-level (e.g. semantic meaning) characteristics. It supports high-level visual inference and perception [1] such as figure/ground analysis and object discovery. It supplies vital cues to methods that generate object proposals [2], which often serve as the starting point for object detection. It is also important for low-level operations, such as object extraction [3], image compositing [4] [5] and spatially varying photo enhancement [6].

Many challenges exist in image segmentation, including the existence of textures and low-frequency appearance variations over objects in an image. Textures bring in high frequency variations (i.e. the Retinex theory [7]); while the low-frequency appearance variations are caused by multiple factors including spatially varying illumination and shading. Both textures and low-frequency variations could make the differences between distant pixels on the same object exceed the differences between nearby pixels on different objects, increasing the difficulty to decide where object boundaries should be. While there have been solutions for suppressing textures using local cues [8], low-frequency variations are harder to remove and would require more global solutions.

A common practice to tackle this challenge is to embed pixels into a new feature space [11], where pixels with similar attributes are pulled closer while pixels with dissimilar attributes stay further away. Clustering pixels in this new feature space would improve segmentation performance if



Fig. 1. Embedding and segmentation results of piecewise flat embedding (PFE). Given an input RGB color image (top left), PFE transforms it into a set of images of embedding channels (bottom), each of which focuses on a subset of characteristics of the original image. A main highlight of our embedding is that the embedding channels tend to be piecewise flat. Two frameworks are tested to segment the image using embedding results, including clustering based segmentation [9] (top middle) and contour driven hierarchical segmentation (top right) [10].

distances in this feature space preserve the intrinsic visual differences as well as disentangle the periphery smooth shading and illumination distractions. Nonetheless, embeddings generated with existing methods still have noticeable smooth variations within same object regions, which often causes clustering-based segmentation algorithms to produce false region boundaries [10]. One effective approach to remove such smooth variations within regions is solving a nonlinear embedding with new regularities.

In this paper, we propose a new nonlinear embedding, called *piecewise flat embedding* (PFE), for image segmentation. This embedding is capable of suppressing variations within segments or clusters while identifying boundaries between them. In the context of image segmentation, since object boundaries only occupy a small percentage of pixels in the whole image, in a locally connected graph, there only

- C. Fang and Y. Yu are with the department of computer science, The University of Hong Kong, Hong Kong. Z. Liao is with the college of computer science, Zhejiang University, Hangzhou.  
E-mail: chwofang@connect.hku.hk; zliao@zju.edu.cn; yizhouy@acm.org

exist a sparse subset of pixel pairs whose pixels come from different object regions. An embedding to pursue the aforementioned property should only have a small subset of pixel pairs maintain sufficiently large distances while distance between any remaining pixel pairs is pushed to zero. According to the theory of sparse signal recovery [12], [13], this embedding problem can be solved via minimizing an objective function regularized with the sparsity of nonzero pairwise pixel differences. Specifically, we attempt to promote sparse solutions by adopting an  $L_{1,p}$ -regularized ( $0 < p \leq 1$ ) energy term in the objective function. This  $L_{1,p}$ -regularized embedding is a generalization of an  $L_1$ -regularized formulation, with extra space for sparsity pursuit and increased degree of nonconvexity as  $p$  becomes smaller. A numerical solution is first developed to solve the  $L_{1,1}$ -regularized objective function by nesting two existing numerical solvers [14], [15]. Inspired by iteratively reweighted  $L_1$  algorithms (IRL1) [16], we further design an iteratively reweighted algorithm based on the numerical solution to the  $L_{1,1}$ -regularized optimization to solve the more generic  $L_{1,p}$ -regularized problem.

It is easy to integrate piecewise flat embedding into existing image segmentation frameworks, including clustering based image segmentation [9] and contour-driven hierarchical segmentation [10]. An example of our embedding results and subsequent clustering based segmentation is shown in Figure 1. We conduct experiment on four popular benchmark datasets, including BSDS500 [10], Stanford Background Dataset (SBD) [17], the precise version [18] of 23-class MSRC [19] and PASCAL Context [20]. Both image segmentation frameworks incorporating PFE achieve state-of-the-art performance comparing to their counterparts.

This paper is an extended version of [21]. New technical contents in this version are summarized as follows.

- The previous  $L_{1,1}$ -regularized objective function is extended to an  $L_{1,p}$ -regularized formulation, which still makes the embedding piecewise flat. An iteratively reweighted numerical algorithm based on nested Bregman iterations is devised to minimize this new objective function.
- The overall numerical solution becomes an order of magnitude faster due to the adoption of the Cholesky Decomposition [22] for directly solving the sparse least-squares problems in the numerical pipeline.
- New initialization schemes and a weighting strategy based on the residual cost of individual embedding channels are devised for piecewise flat embedding to achieve improved performance in image segmentation.
- Segmentation algorithms integrating our embedding produce state-of-the-art performance on three benchmark datasets (BSDS500, SBD, MSRC and PASCAL Context).

## 2 RELATED WORK

**Image Segmentation** A comprehensive summarization on segmentation methods has been given in [3]. Here we discuss five types of segmentation techniques which are closely related to our method. If pixels in an image are taken as a set of unordered data samples, most clustering algorithms, such as K-means [23], Gaussian Mixture Models [24] and MeanShift [25], can be used for image segmentation.

Graph partition is also a widely used approach. Modeling the 2D pixel grid of an image as a Markov random field, graphcut algorithms [26], [27], [28] have been developed to solve binary or multi-label image segmentation efficiently. Graph based segmentation [29] is another efficient method based on greedily deciding the existence of boundaries between pairs of regions. Spectral embedding [11] projects pixels into a new feature space where similar pairs of pixels stay closer than dissimilar pairs, and solves a normalized graph partition problem. Channels in a spectral embedding provide not only better features for clustering based segmentation [9], but also clearer global boundary information [30].

Gradient based methods form another representative approach in image segmentation. Examples include segmentation based on the watershed transform [31]. In [32], OWT-UCM transforms a boundary probability map to a hierarchical segmentation, where oriented watershed transform (OWT) is designed to remove noises arising from the standard watershed algorithm, and ultrametric contour map (UCM) combines closed, non-self-intersecting weighted contour information. With the recent developments in contour detection [8], [30], [33], [34], [35], OWT-UCM remains a favorable choice for image segmentation [2], [10]. Starting from small superpixels, INSCRA [36] generates hierarchical segmentation with the help of a sequence of cascaded discriminative classifiers. LEP [37] is a more recent hierarchical segmentation algorithm, which is inspired by the least effort principle and models the amount of effort involved in tracing boundaries by human.

The above segmentation methods are not related to the sparsity theory. However the  $L_1$  norm has been commonly adopted in the level set method [38], [39] which models an image as a scalar function defined on a 2D plane. It extracts image segments as implicit regions whose boundary curve is an isocontour of the scalar function.

**Manifold Learning** To cope with the "curse of dimensionality", various manifold learning algorithms have been proposed for nonlinear dimension reduction that preserves structural information. These algorithms roughly fall into two categories, local methods and global methods. Local methods, such as LLE [40] and Laplacian Eigenmaps [41], attempt to preserve local structures among data points. t-SNE [42], [43], an extension of SNE [44], generates pleasant embedding results for the visualization of high dimensional data. GNMF [45] is another local method that proposes a graph regularized objective function to take into account both the reconstruction loss and local pairwise variation cost.

Global methods, such as Isomap [46] and structure preserving embedding [47], attempt to preserve local and global relationships among all data points. Sparsity constraints have been considered in SMCE [48] and Sparse Embedding [49]. SMCE constructs neighborhood relationships via selecting neighbors from the same manifold for each data point, which is solved as a sparse optimization problem. It then follows the spectral method to compute embedding and clustering results. Sparse Embedding performs simultaneous dimension reduction and dictionary learning by learning a transformation from the original



Fig. 2. Sparsity of boundary pixels and edges crossing region boundaries in a locally connected graph. The percentage of boundary pixels in the image on the left is 1.85%. The image on the right visualize the percentage of locally connected edges crossing region boundaries. The percentage of such edges in the image is 5.07% if every pixel is connected to other pixels in a  $11 \times 11$  neighborhood.

high-dimensional space to a low-dimensional space while preserving sparse structures. SSC proposed in [50] attempts to learn a sparse and global affinity matrix through representing every sample with a few samples in the same subspace. The more the reference sample contributes to reconstructing the query sample, the higher similarity they possess. GraphEncoder [51] tries to embed affinity matrix into feature space directly in the prototype of autoencoder. [52] proposes to embed different types of data (image and text) to a unified space with the help of deep learning technologies. Our method differs from these embedding techniques in the sense that we directly minimize a global objective function formulated using  $L_{1,p}$  regularization without dictionary learning.

### 3 PIECEWISE FLAT EMBEDDING

Let us consider the problem of dividing an image into regions containing pixels with similar low-level/high-level features. We first construct a locally connected graph  $G = (V, E)$ , where  $V$  represents the set of pixels and  $E$  represents edges connecting pixels within a neighborhood size. For the example shown in Figure 2, with neighborhood size  $11 \times 11$ , among all the edges in the graph, only a very small fraction (around 5%) of them are connections that straddle cross object boundaries – the majority are between pixels from the same region. This indicates region boundaries might be discovered as the solution to an energy minimization problem with sparsity regularization.

Further, we would like to constrain the feature embedding of pixels from the same region to lie as tightly with one another as possible, therefore achieving the goal of piecewise “flat” embedding. This piecewise flatness property matters. From one point of view it reduces the intra-class variations of raw pixel values within image segments, for reasons explained earlier. From another point of view, it aims to factorize out a *piecewise smooth* component, which is known as an intrinsic component of pixel values from image formation, and pursues a feature embedding that captures a set of *piecewise constant* representations. This section will describe our formulation of the problem and a numerical solution to it.

#### 3.1 Problem Definition

Given  $n$  data points  $\mathbf{X} = \{\mathbf{x}_1, \dots, \mathbf{x}_n\}$  in  $R^m$ , we would like to embed them into a new  $d$ -dimension space  $R^d$ . Let

$\mathbf{Y} = [\mathbf{y}_1, \dots, \mathbf{y}_n]^T$  be the  $n \times d$  data matrix in the new space, where  $\mathbf{y}_k^T$  is the  $k$ -th row of  $\mathbf{Y}$ , representing the  $d$  coordinates of the  $k$ -th data point in the new space. PFE is to find an embedding  $\mathbf{Y}$  that achieves the sparsity, or the piecewise flat property by minimizing the following objective function,

$$\min_{\mathbf{Y}} \sum_{ij} \|W_{ij}(\mathbf{y}_i - \mathbf{y}_j)\|_1^p \quad s.t. \quad \mathbf{Y}^T \mathbf{D} \mathbf{Y} = \mathbf{I}, \quad (1)$$

where  $0 < p \leq 1$ ,  $\mathbf{W} = \{W_{ij}\}$  is the affinity matrix, and  $\mathbf{D}$  is the diagonal weight matrix with  $D_{ii} = \sum_j W_{ji}$ . Our embedding formulation is inspired by Normalized Cuts [11] and Laplacian Eigenmaps (LE) [41], which is defined as follows:

$$\min_{\mathbf{Y}} \sum_{ij} W_{ij} \|\mathbf{y}_i - \mathbf{y}_j\|_2^2 \quad s.t. \quad \mathbf{Y}^T \mathbf{D} \mathbf{Y} = \mathbf{I}, \quad (2)$$

where  $\mathbf{W}$  and  $\mathbf{D}$  are defined in the same way.

Note  $\mathbf{W}$  is a symmetric sparse matrix, so we can rewrite the problem formulation in (1) as the following,

$$\min_{\mathbf{Y}} \|(\mathbf{M} \mathbf{Y})^T\|_{1,p}^p \quad s.t. \quad \mathbf{Y}^T \mathbf{D} \mathbf{Y} = \mathbf{I}, \quad (3)$$

where  $\mathbf{M} = \{M_{ij}\}$  is a  $t \times n$  matrix,  $M_{ki} = W_{ij} = -M_{kj}$  are for data points  $\mathbf{x}_i$  and  $\mathbf{x}_j$  that form the  $k$ -th non-zero entry of the affinity matrix, and  $t$  is the total number of non-zero entries.  $\|\mathbf{A}\|_{q,p} = (\sum_j (\sum_i |A_{ij}|^q)^{p/q})^{1/p}$  is the  $L_{q,p}$  norm of matrix  $\mathbf{A}$ .

Similarly, the Laplacian Eigenmaps formulation (2) can be rewritten as follows,

$$\min_{\mathbf{Y}} \|(\mathbf{M}' \mathbf{Y})^T\|_{2,2}^2 \quad s.t. \quad \mathbf{Y}^T \mathbf{D} \mathbf{Y} = \mathbf{I}, \quad (4)$$

where  $\mathbf{M}'$  is a  $t \times n$  matrix,  $M'_{ki} = W_{ij}^{1/2} = -M'_{kj}$  are for data points  $\mathbf{x}_i$  and  $\mathbf{x}_j$  that form the  $k$ -th non-zero entry of  $\mathbf{W}$ .

Although (3) and (4) are similar, the most obvious difference is that we use the  $L_{1,p}$  norm in (3) while the formulation of Laplacian Eigenmaps inherits a common trait of mainstream embedding methods, which is the use of the squared  $L_{2,2}$  norm in the objective function. In fact, such a small difference has the following important implication. The  $L_{1,p}$  norm promotes sparse solutions while the  $L_{2,2}$  norm does not. A sparse solution implies that, among all locally connected point pairs, there only exists a sparse subset of point pairs whose distances in the new space are sufficiently large, and the distances between the rest of the point pairs are almost zero. Such a sparse solution suggests points with a large distance in the new space should belong to different clusters and points with a very small distance in the new space should belong to the same cluster. Therefore, performing clustering in the new space becomes a straightforward process. On the other hand, although the affinity matrix in (4) attempts to move points with similar attributes closer in the new space, the resulting pairwise distances in the new space still follows a relatively smooth distribution, and the distinction between similar points and dissimilar points is not as clear as in our results.

In the context of image segmentation, a sparse solution to (3) means there only exist a sparse subset of locally connected pixel pairs whose pairwise difference in the new

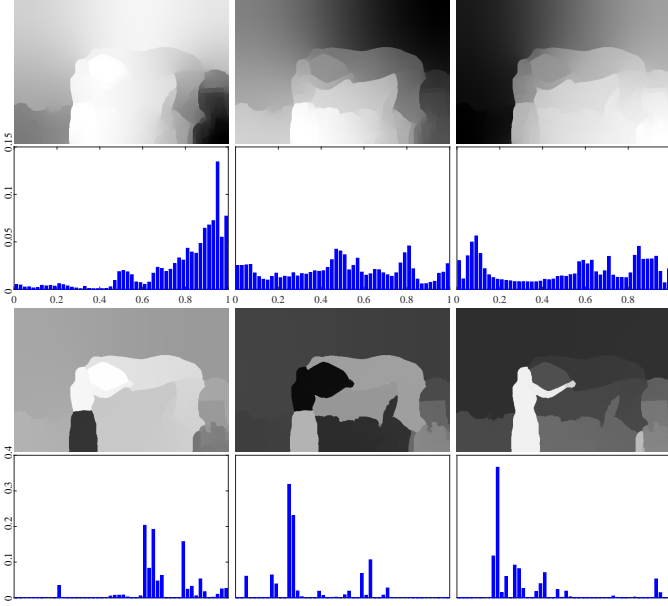


Fig. 3. Laplacian Eigenmap (top row) and PFE (third row) embedding results, and histograms of each embedding channel. PFE channels are almost piecewise constant while LE channels are piecewise smooth. Because of the adopted  $L_{1,p}$  norm, the histograms of our results are much sparser than those of Laplacian Eigenmaps.

space,  $\mathbf{y}_i - \mathbf{y}_j$ , remains sufficiently different from zero. Since the affinity  $W_{ij}$  appears together with  $\|\mathbf{y}_i - \mathbf{y}_j\|_1$ , a large affinity forces  $\|\mathbf{y}_i - \mathbf{y}_j\|_1$  to approach zero and  $\|\mathbf{y}_i - \mathbf{y}_j\|_1$  becomes nonzero only when the affinity is relatively small. On the other hand, pixel pairs crossing region boundaries typically have smaller affinities than those from the same region. Therefore, the sparse solution to (3) should be capable of facilitating the discovery of region boundaries. At the interior of a region,  $\mathbf{y}_i - \mathbf{y}_j$  would be most likely zero due to the large affinity between them. This implies each embedding channel has an almost constant value inside every region, hence, the name *piecewise flat embedding*.

A visual comparison between our  $L_{1,1}$ -regularized PFE and Laplacian Eigenmaps are shown in Figure 3, where each image represents pixelwise values of one embedding channel and the histogram below each image represents the pixel distribution of that embedding channel. According to the results in this figure, PFE channels are almost piecewise constant and their histograms are much sparser than those of Laplacian Eigenmaps, which still possess obvious nonzero gradients within image regions.

**Connection with Total Variation** The discretized total variation energy has been frequently used in image denoising and restoration [53]. Its energy function is as below,

$$\min_{\mathbf{u}} \sum_i \sqrt{(\nabla_x \mathbf{u})_i^2 + (\nabla_y \mathbf{u})_i^2} \quad s.t. \quad \mathbf{u} = \mathbf{u}_0 \quad (5)$$

where  $\mathbf{u}_0$  is usually the input image and  $\mathbf{u}$  represents the restored image. It is easy to derive an  $L_1$ -norm counterpart of total variation from (5),

$$\min_{\mathbf{u}} \|\nabla_x \mathbf{u}\|_1 + \|\nabla_y \mathbf{u}\|_1 \quad s.t. \quad \mathbf{u} = \mathbf{u}_0 \quad (6)$$

When  $p = 1$ , our  $L_{1,1}$ -regularized energy term may appear similar to (6). However, there exist crucial differences

between the two. First, each pairwise difference in our formulation is weighted by an affinity, which makes similar pixels even closer in the embedding space, while all components in total variation formulations are equally weighted. Second, our formulation allows direct interaction between pixels further apart by setting up connections between pixels falling into each other's neighborhood, which could be much larger than  $3 \times 3$ , while a discretized gradient operator in total variation formulations only involves pixels within a  $3 \times 3$  neighborhood. These aspects of our formulation further improve the sparsity of the solution. Furthermore, the data term in total variation formulations is replaced with the orthogonality constraint in our formulation. The removal of the data term allows the embedding space to be more independent from the space of the input data. For example, the embedding space can have a different dimensionality and the embedding channels do not have to approximate the input data.

### 3.2 Numerical Solution

In the following, we first present an iterative numerical solution for a special case of the problem in (3), where the  $L_{1,1}$  norm is used instead of the more general  $L_{1,p}$  norm. A new initialization scheme for this iterative solution is devised. Then a numerical solution for the original problem in (3) with the  $L_{1,p}$  norm is introduced as an iteratively reweighted version of the special-case solution.

#### 3.2.1 Solution to $L_{1,1}$ -regularized Objective Function

By setting  $p = 1$  in (3), we obtain the  $L_{1,1}$ -regularized objective function as follows,

$$\min_{\mathbf{Y}} \|\mathbf{M}\mathbf{Y}\|_{1,1} \quad s.t. \quad \mathbf{Y}^T \mathbf{D} \mathbf{Y} = \mathbf{I}. \quad (7)$$

Solving this problem is challenging as it consists of  $L_{1,1}$  regularization and an orthogonality constraint while most of existing numerical algorithms can only handle one of them. Here we present a numerical solution by nesting two existing solvers that handle  $L_1$ -regularized optimization and orthogonality constraints respectively. This solution is later accelerated with a two-stage strategy that relaxes the orthogonality constraint.

Since the objective function in (7) is convex, we apply the Splitting Orthogonality Constraint (SOC) algorithm in [15]. Following the derivation of the SOC algorithm, we define  $\mathbf{P} = \mathbf{D}^{1/2} \mathbf{Y}$ , and rewrite (7) as,

$$\min_{\mathbf{Y}} \|\mathbf{M}\mathbf{Y}\|_{1,1} \quad s.t. \quad \mathbf{D}^{1/2} \mathbf{Y} = \mathbf{P}, \quad \mathbf{P}^T \mathbf{P} = \mathbf{I}, \quad (8)$$

which can be iteratively solved using Bregman iterations [54] as follows:

- (a)  $\mathbf{Y}^{(k+1)} = \arg \min_{\mathbf{Y}} \|\mathbf{M}\mathbf{Y}\|_{1,1} + \frac{r}{2} \|\mathbf{D}^{1/2} \mathbf{Y} - \mathbf{P}^{(k)} + \mathbf{B}^{(k)}\|_{2,2}^2;$
- (b)  $\mathbf{P}^{(k+1)} = \arg \min_{\mathbf{P}} \|\mathbf{P} - (\mathbf{D}^{1/2} \mathbf{Y}^{(k+1)} + \mathbf{B}^{(k)})\|_{2,2}^2,$   
s.t.  $\mathbf{P}^T \mathbf{P} = \mathbf{I};$
- (c)  $\mathbf{B}^{(k+1)} = \mathbf{B}^{(k)} + \mathbf{D}^{1/2} \mathbf{Y}^{(k+1)} - \mathbf{P}^{(k+1)};$

where  $\mathbf{B}$  is an auxiliary matrix, and  $\mathbf{B}^{(0)} = \mathbf{0}$ .



According to Theorem 2.1 in [15], the spherically constrained problem in step (b) has the following closed form solution:

$$\begin{aligned} \mathbf{D}^{1/2} \mathbf{Y}^{(k+1)} + \mathbf{B}^{(k)} &= \mathbf{U} \Sigma_{n \times d} \mathbf{V}^T, \\ \mathbf{P}^{(k+1)} &= \mathbf{U} \mathbf{I}_{n \times d} \mathbf{V}^T, \end{aligned} \quad (9)$$

where  $\mathbf{U}$  and  $\mathbf{V}$  are matrices with orthogonal columns from the SVD decomposition in the first step.

The subproblem in step (a) of the above numerical solution inherits the  $L_{1,1}$ -regularized energy term from (7). There exist many numerical solutions for optimization problems with  $L_1$  regularization. For reasons discussed later, we choose to apply the Split Bregman algorithm in [14] to solve the subproblem in step (a). By introducing auxiliary variables, the Split Bregman algorithm solves an  $L_1$ -regularized optimization iteratively by transforming the original optimization into a series of differentiable unconstrained convex optimization problems. The definition of any convex optimization in the series depends on the auxiliary variables passed from the previous iteration, and convergence can be achieved within a relatively small number of iterations. Detailed solution to the  $L_{1,1}$ -regularized problem in step (a) is enclosed in Appendix A.

**Two-Stage Implementation** In practice, we run the following two-stage implementation to obtain a high-quality solution more efficiently.

*Stage I* This stage implements the full numerical solution with nested Bregman iterations. A large penalty coefficient for the orthogonality constraint is used. The outer loop makes different dimensions of the embedded data orthogonal to each other to remove redundancy among them. This is important in avoiding naive solutions with highly redundant or even duplicate dimensions.

However, orthogonality is a highly non-convex constraint that prevents the objective function in (7) from settling into a truly low-energy state; and more important, it is not absolutely necessary for us to pursue an embedding whose dimensions are strictly orthogonal as long as there is not too much redundancy across different dimensions. Therefore, following a few iterations of the full numerical solution, we relax the orthogonality constraint in a second stage.

*Stage II* This stage only executes the Bregman iterations in the inner loop without performing the SVD in the outer loop to strictly enforce orthogonality. Such relaxation of the orthogonality constraint allows the objective function to reach a lower energy.

Figure 4 shows an example of the energy curve during Stage I and Stage II. It verifies our two-stage scheme can reach a lower energy than a single-stage one.

**Residual-Based Channel Weighting** For the sake of efficiency, we run the numerical procedure in each stage for a predefined number of iterations instead of waiting until the empirical error of every embedding channel falls below a predefined tolerance  $\epsilon$ . Thus the obtained embedding channels differ from each other with respect to the degree of convergence. To moderate the effect of such early termination, we devise the following weighting scheme based on

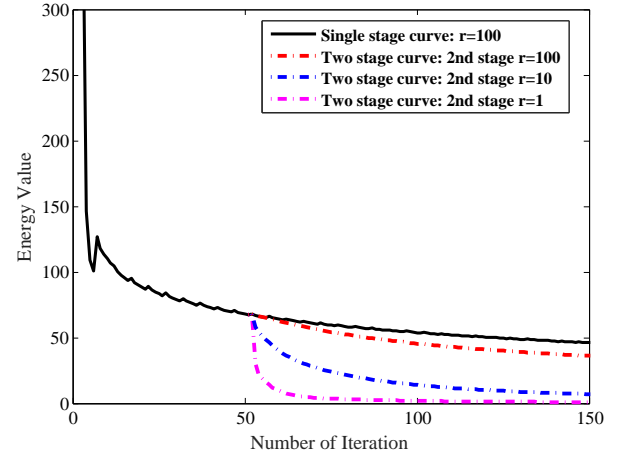


Fig. 4. Energy curves. The black curve shows how the energy decreases with regular single-stage Bregman iterations with  $\lambda = 1000, r = 100$ . The dashed curves show how energy evolves with our 2-stage algorithm. The first stage is the same as the black curve. The second stage starts from iteration 50. The three dashed curves show varying convergence rates using different parameter values ( $r = 100, 10, 1$  respectively for the red, blue and pink curves.)



Fig. 5. Comparison of segmentations using piecewise flat embedding without (middle) and with (right) residual-based channel weighting. Left are input images.

the residual cost of the objective function with respect to each embedding channel,

$$\begin{aligned} \eta_v &= \sqrt{\frac{\|\mathbf{M}\mathbf{Y}_v\|_1}{\|\mathbf{D}^{1/2}\mathbf{Y}_v\|_2}}, \\ \hat{\mathbf{Y}}_v &= \text{normalize}(\mathbf{Y}_v)/\eta_v, \end{aligned} \quad (10)$$

where  $\mathbf{Y}_v$  and  $\hat{\mathbf{Y}}_v$  are the  $v$ -th columns of  $\mathbf{Y}$  obtained at the end of Stage II and the final embedding  $\hat{\mathbf{Y}}$  respectively. This weighting scheme makes the importance of a channel lower if it has a larger residual cost. A comparison of PFE-based segmentations with and without residual-based channel weighting are shown in Figure 5, where segmentation results with residual-based channel weighting are clearly better.

### 3.2.2 Solution to $L_{1,p}$ -regularized Objective Function

To leverage algorithms for handling simpler objective functions when a more sophisticated objective function is optimized, a class of numerical methods based on iterative reweighting has been previously developed. These methods iteratively optimize a smooth or nonsmooth convex objective function dynamically weighted by coefficients



Fig. 6. Comparison of PFE-based segmentations with  $L_{1,1}$  (middle) and  $L_{1,0.8}$  (right) regularization. Left are input images.

evaluated from the previous iteration. For instance, IRLS [55], [56] solves iteratively reweighted quadratic problems while IRL1 [57] solves iteratively reweighted  $L_1$ -regularized problems. Algorithms using iterative reweighting have been recently summarized in [16]. Inspired by such methods, we develop a method based on iterative reweighting to solve the  $L_{1,p}$ -regularized problem in (3).

As done for the  $L_{1,1}$ -regularized problem in (7), the  $L_{1,p}$ -regularized problem in (3) is also solved in two stages. The first stage of the numerical procedures for solving these two problems is completely the same. The result from the first stage initializes the second stage. In the second stage, we revise the objective function in step (a) of the procedure solving (7) as follows,

$$\mathbf{Y} = \arg \min_{\mathbf{Y}} \|(\mathbf{M}\mathbf{Y})^T\|_{1,p}^p + \frac{r}{2}\Psi(\mathbf{Y}), \quad (11)$$

where  $\Psi(\mathbf{Y}) = \|\mathbf{D}^{1/2}\mathbf{Y} - \mathbf{P} + \mathbf{B}\|_{2,2}^2$ ,  $\mathbf{P}$  and  $\mathbf{B}$  are obtained from the last outer iteration of the first stage.

We apply the majorization-minimization algorithm [16] to solve the problem in (11). A Detail description is enclosed in Appendix B.

Residual-based weighting introduced earlier can still be applied to individual channels of  $\mathbf{Y}^{(k+1)}$  obtained in the first step to improve segmentation performance. Define the result from residual-based weighting as  $\hat{\mathbf{Y}}^{(k+1)}$ . Then the second step of the algorithm in Appendix B is revised as follows,

$$w_i^{k+1} = \max(\alpha \|\mathbf{m}_i^T \hat{\mathbf{Y}}^{(k+1)}\|_1, \varepsilon)^{p-1}, \quad (12)$$

where  $\alpha$  is a constant. We experimentally found that the revised iterations can converge when  $0 < \alpha \leq 50$ .

A comparison of segmentations obtained through  $L_{1,1}$  regularization and  $L_{1,p}$  ( $p = 0.8$ ) regularization are shown in Figure 6.  $L_{1,0.8}$  regularization gives rise to more accurate results.

**Parameter Setting** For methods developed in this paper, we select parameters as follows. In Stage I, we set the maximum number of outer iterations to 5 and the number of inner iterations to 8. In Stage II of the algorithm optimizing the  $L_{1,1}$ -regularized objective function in (7), the maximum number of iterations is set to 40. For the  $L_{1,p}$ -regularized objective function in (3), there still exists a double loop in the second stage due to iterative reweighting. We set the maximum number of outer iterations to 5 and the number of inner iterations to 20 or less. The parameter setting for  $\alpha$ ,  $\varepsilon$ ,  $\lambda$  and  $r$  will be given in the following section on image segmentation. Figure 7 shows a few embedding results.

## 4 IMAGE SEGMENTATION USING PIECEWISE FLAT EMBEDDING

An image with resolution  $w \times h$  gives rise to a set of  $n = w \times h$  data points. By computing an affinity value between neighboring pixels, we have a locally connected graph (with  $n$  nodes), where edge weights can be represented with a  $n \times n$  sparse affinity matrix  $\mathbf{W}$ . A piecewise flat embedding of these data points in a new  $d$ -dimensional space can be computed using the numerical algorithms in the previous section. We have integrated such embedding results in two popular image segmentation frameworks. Figure 8 illustrates our segmentation pipeline.

### 4.1 Segmentation by Clustering

The first segmentation framework we have considered is based on spectral clustering [9]. Spectral clustering first computes a set of generalized eigenvectors from the locally connected graph. The elements in these eigenvectors corresponding to the same pixel form a  $d$ -dimensional feature vector at that pixel. It then runs standard clustering, such as K-means, on the pixelwise feature vectors. A variant of spectral clustering, named weighted spectral clustering, reweights the  $i$ -th feature coordinates by  $1/\sqrt{\lambda_i}$ , where  $\lambda_i$  is the eigenvalue corresponding to the  $i$ -th eigenvector.

Our revised clustering-based segmentation simply replaces the eigenvectors in spectral clustering with the channels in our embedding. That is, each row of the matrix  $\mathbf{Y}$  becomes the  $d$ -dimensional feature vector of the corresponding pixel. Since our embedding is not a spectral one, instead of eigenvalues, we make use of the channel-wise residual cost in our channel weighting scheme defined in (10). Afterwards, we still perform K-means clustering on the original or weighted channels.

Since our embedding is piecewise flat, pixels of the same region are tightly distributed in the feature space. In contrast, existing embedding techniques, such as Laplacian Eigenmaps, do not share this property. A Laplacian eigenmap is obtained by minimizing the smooth  $L_{2,2}$ -regularized objective function in (4). The resulting eigenmaps are piecewise smooth but not piecewise flat. Therefore pixels from the same region may still have reasonably large distances among them in the feature space, and may not be grouped together into the same cluster. This is the reason why large or elongated regions are often broken up into pieces in segmentation results based on spectral clustering.

### 4.2 Contour-Driven Hierarchical Segmentation

One strategy avoiding the drawback of spectral clustering, called OWT-UCM [10], derives global contour information from the eigenmaps computed from the affinity matrix, and then forms segments with respect to contours using hierarchical agglomerative clustering. The hierarchical tree structure built during clustering makes it flexible to choose a segmentation granularity. To make the algorithm robust, this method also combines local edges with global contours when constructing the contour probability map. Our contour-driven segmentation follows the same pipeline, except that global contours are extracted from the channels of our embedding instead of the eigenmaps.



Fig. 7. Examples of our piecewise flat embedding. For each row, leftmost column is input image; the rest are four embedding channels. Notice each embedding channel exhibits clear geometric property of piecewise flatness.

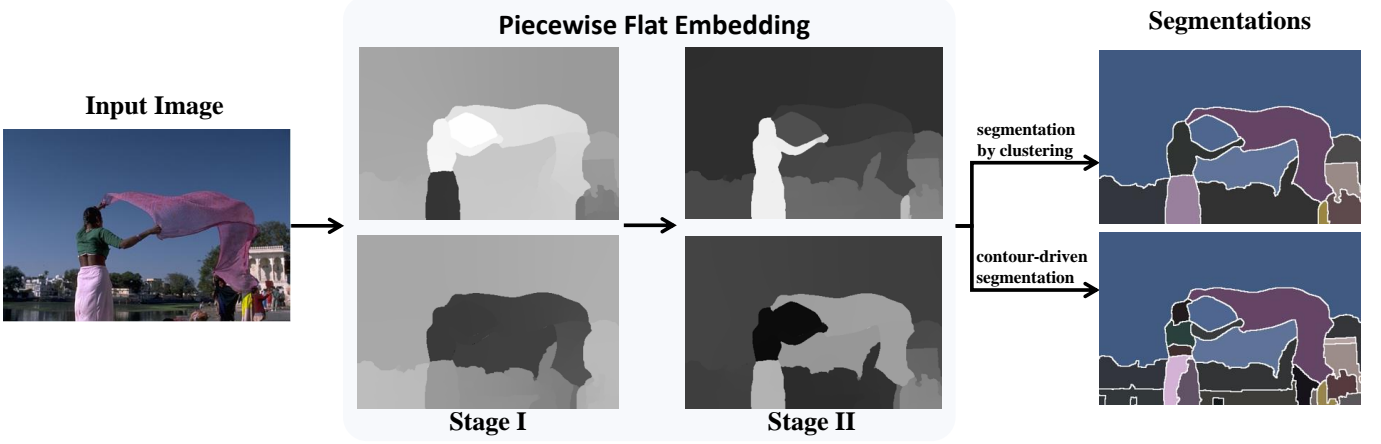


Fig. 8. Image segmentation pipeline. Given an input image, our method generates a piecewise flat embedding from an affinity matrix of the image in a two-stage optimization. The channels in the embedding are used for image segmentation either in a clustering-based method, or a contour-driven hierarchical method.

Again, since our embedding is piecewise flat, channels in our embedding have almost zero gradients everywhere except at region contours where gradients have a large magnitude. Contour maps extracted from our embedding are both clear and clean without many spurious edges.

#### 4.3 PFE Initialization for Image Segmentation

Initialization plays an important role for the iterative algorithm to converge to a local minimum. As in [21], we proposed an initialization scheme based on Gaussian Mixture Models: we fit a Gaussian model to each of the  $2^d$  clusters, and use the Gaussians to generate  $2^d$  density maps. the density maps are then encoded into  $d$  images as the initial channels of piecewise flat embedding. Suppose the

Gaussians have been ordered into a linear sequence. Each initial channel is formed by summing up  $2^{d-1}$  density maps and subtracting the mean from every pixel. For example, the first channel records the mixed density of the first half of the Gaussians; then we divide the sequence in the middle into two equal subsequences, and the second channel records the mixed density of the first half of the Gaussians in both subsequences. Once the initial  $\mathbf{Y}$  has been set,  $\mathbf{P}$  is initialized with an orthogonalized version of  $\mathbf{D}^{1/2}\mathbf{Y}$  using (9). An example of initialization is shown in Figure 9.

However, it is neither efficient nor robust as GMM was implemented using expectation maximization iterations and initialized randomly. Here we devise two more effective initialization schemes: hierarchical clustering, and weighted spectral clustering (WSC). 1) For hierarchical clustering, we



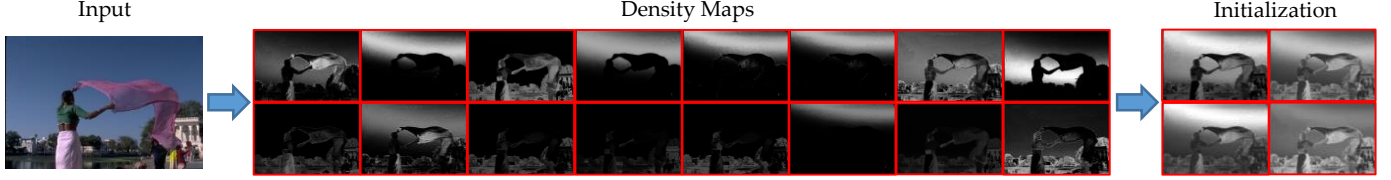


Fig. 9. Initialization. The 16 probability density maps (**Middle**) are defined with Gaussian models of 16 pixel clusters formed via spectral clustering. Each channel (image) in the initialization (**Right**) represents the mixed density of 8 Gaussian models. Specifically, the first channel (ordered from left to right and top to bottom) mixes the 8 density maps in the first row; the second channel mixes the first 4 density maps in both rows; the third channel mixes the 1st, 2nd, 5th and 6th density maps in both rows; and the fourth channel mixes the 1st, 3rd, 5th and 7th density maps in both rows.

use finest level superpixel from [29], representing each superpixel with its average RGB values, and agglomeratively merging them until  $2^d$  clusters are left. 2) For WSC, we employ RGB values to compute the affinity matrix and cluster pixels into  $2^d$  groups with the weighted spectral clustering method [58]. Our final model adopts this *WSC*-based initialization scheme, and we will evaluate and compare the performance of the three schemes in later section.

TABLE 1

Comparison of Normalized Cut (NCut), spectral clustering (SC), weighted spectral clustering (WSC) and our method (swPFE<sub>0.8</sub>) on BSDS500 using affinity in the original Normalized Cut.

method	$F_{op}$		Covering		PRI		VI	
	fixed	dynamic	fixed	dynamic	fixed	dynamic	fixed	dynamic
NCut	0.126	0.194	0.333	0.405	0.748	0.757	2.772	2.388
SC	0.146	0.210	0.363	0.445	0.751	<b>0.768</b>	2.680	2.243
WSC [58]	0.160	0.206	0.369	0.444	0.750	0.767	2.628	2.207
swPFE <sub>0.8</sub>	<b>0.247</b>	<b>0.256</b>	<b>0.500</b>	<b>0.518</b>	<b>0.753</b>	0.758	<b>1.972</b>	<b>1.863</b>

TABLE 2

Comparison between existing segmentation-by-clustering methods (spectral clustering, weighted spectral clustering) and our method (swPFE<sub>0.8</sub>) on BSDS500 using affinity computed from local contour information. 'dyn' stands for the *dynamic* clustering scheme.

method	$F_b$		$F_{op}$		Covering		PRI		VI	
	fixed	dyn	fixed	dyn	fixed	dyn	fixed	dyn	fixed	dyn
SC	0.599	0.641	0.178	0.257	0.378	0.490	0.764	0.788	2.517	1.988
WSC [58]	0.599	0.643	0.185	0.259	0.378	0.479	0.765	0.784	2.496	1.980
swPFE <sub>0.8</sub>	<b>0.704</b>	<b>0.716</b>	<b>0.426</b>	<b>0.428</b>	<b>0.643</b>	<b>0.653</b>	<b>0.847</b>	<b>0.848</b>	<b>1.388</b>	<b>1.343</b>

## 5 EXPERIMENTS

We have conducted experiments within the two aforementioned segmentation frameworks: (a) segmentation by clustering and (b) contour-driven hierarchical segmentation, and compared revised segmentation algorithms incorporating our embedding against the original and other existing algorithms.

We first incorporate our piecewise flat embedding into the clustering-based segmentation approach, and compare it against three existing spectral methods. Two types of affinity matrices are used: the affinity used in the original Normalized Cut algorithm [11], and that using local boundary probability [59]. Table 1 shows comparison results using the original Normalized Cut affinity. Table 2 shows comparison results using the affinity computed from local contour information.

Clustering-based segmentation using K-means need to specify the number of clusters. We used the following two

schemes during performance testing: the *fixed* scheme and the *dynamic* scheme. The *fixed* scheme uses the number of segments provided by the groundtruth segmentation. If there are multiple groundtruth segmentations, we run the algorithm with the number of segments for every groundtruth segmentation, and take the average. The *dynamic* scheme sets the number of segments to odd numbers between 5 and 25 (empirically), and chooses the one with the best performance. For methods that require multiple NCut eigenvectors, we run each method using 4, 8, and 16 eigenvectors respectively, and take the one with the highest performance.

We have also incorporated piecewise flat embedding into contour-driven hierarchical segmentation following the pipeline in gPb-owt-ucm [10] and MCG [2]. In our revised algorithms, we replace the eigenmaps with our piecewise smooth embedding. We have also conducted segmentation experiments by additionally replacing the local contours in gPb-owt-ucm [10] with those computed from Deep Boundaries (DB) [59]. We compare the segmentation performance of our revised algorithms with the original algorithms and a number of existing algorithms. The comparison results are shown in Tables 3, 4, and 6.

**Metrics** The results are evaluated using four standard criteria:  $F$  measure for boundaries ( $F_b$ ), Segmentation Covering (Covering), Probabilistic Rand Index (PRI), and Variation of Information (VI) described in the BSDS segmentation benchmark [10], plus another widely used benchmark metrics,  $F$  measure for objects and parts ( $F_{op}$ ) proposed in [60]. We use threshold range  $\{\frac{x}{101} | x = 0, 1, \dots, 100\}$  for all UCM based methods.

**Datasets** Experiments and comparison are conducted on the following 3 benchmark datasets:

- **BSDS500** [10]: 200 training, 100 validation and 200 testing images. 5-10 groundtruth segmentations are annotated by different subjects for each image. Image size is  $321 \times 481$  or  $481 \times 321$ .
- **SBD**: Stanford Background Dataset [17], 715 images of outdoor scenes.
- **MSRC** [19]: 591 images and 23 object classes. Precise groundtruth images are provided in [18].
- **PASCAL Context** [20]: an annotation of PASCAL VOC 2010 [61] containing 10,103 images. 459 classes of objects are labeled. It is split into 4,998 training images, 2,607 validation images and 2,498 testing images in [62].



TABLE 3

Segmentation performance on BSDS500. Our methods ('swPFE<sub>0.8</sub>+mPb', 'swPFE<sub>0.8</sub>+MCG', 'swPFE<sub>0.8</sub>+DB' and 'swPFE<sub>0.8</sub>+COB') perform favorably over their counterparts (gPb-owt-ucm, MCG, 'LE+DB' and COB respectively) and previous work. Segmentations based on LE and our default PFE (swPFE<sub>0.8</sub>), as well as DB, are all implemented in the OWT-UCM (contour-driven hierarchical segmentation) framework [10], [32]. The integration of powerful local boundary cues, i.e. DB [59], is critical for our method to achieve state-of-the-art performance in this task.

method	$F_b$		$F_{op}$		Covering		PRI		VI	
	ODS	OIS	ODS	OIS	ODS	OIS	ODS	OIS	ODS	OIS
MS-NCut [63]	0.64	0.68	0.213	0.270	0.45	0.53	0.78	0.80	2.23	1.89
Mean Shift [25]	0.64	0.68	0.229	0.292	0.54	0.58	0.79	0.81	1.85	1.64
Hoiem [64]	-	-	-	-	0.56	0.60	0.80	0.77	1.78	1.66
ISCRA [36]	0.717	0.752	0.352	0.418	0.592	0.660	0.821	0.857	1.605	1.415
LEP [37]	0.754	0.789	0.422	0.466	0.629	0.677	0.836	0.864	1.468	1.325
gPb-owt-ucm [10]	0.729	0.755	0.348	0.385	0.587	0.646	0.828	0.855	1.690	1.476
swPFE <sub>0.8</sub> +mPb	0.723	0.752	0.364	0.411	0.612	0.669	0.830	0.866	1.565	1.386
MCG [2]	0.744	0.777	0.379	0.433	0.613	0.663	0.832	0.861	1.568	1.390
swPFE <sub>0.8</sub> +MCG	0.747	0.779	0.397	0.448	0.622	0.679	0.838	0.870	1.557	1.365
DB [59]	<b>0.809</b>	0.832	0.437	0.491	0.663	0.714	0.857	0.886	1.387	1.211
LE+DB	<b>0.809</b>	<b>0.833</b>	0.445	0.500	0.665	0.716	0.858	0.886	1.365	1.197
swPFE <sub>0.8</sub> +DB	<b>0.809</b>	0.832	<b>0.463</b>	<b>0.514</b>	<b>0.680</b>	<b>0.722</b>	<b>0.860</b>	<b>0.887</b>	<b>1.293</b>	<b>1.145</b>
COB [62]	0.782	0.808	0.414	0.464	0.664	0.712	0.854	0.886	1.380	1.222
LE+COB	0.782	0.809	0.413	0.462	0.656	0.706	0.854	0.882	1.384	1.245
swPFE <sub>0.8</sub> +COB	0.787	0.810	0.430	0.485	0.670	0.718	0.858	0.887	1.337	1.182

**Implementation** When computing our piecewise flat embedding in the clustering-based segmentation, we set the parameters  $\lambda$  and  $r$  to 40000 and 600 respectively in stage I, and  $r$  is reduced to 10 in stage II.  $\alpha = 0.1$ ,  $\varepsilon = 10^{-5}$ , and the neighborhood size is set to  $7 \times 7$  in PFE computed using the  $L_{1,1}$ -regularized and  $L_{1,p}$ -regularized objective functions, respectively. When computing our piecewise flat embedding in the contour-driven hierarchical segmentation, we set the parameters  $\lambda$  and  $r$  to 4000 and 600 respectively in stage I, and reduce  $r$  to 10 in stage II.  $\alpha = 50$ ,  $\varepsilon = 10^{-2}$ , and the neighborhood size is set to  $11 \times 11$ .

**Notations** For clarity, we define the following expression to differentiate among variants of piecewise flat embedding used in image segmentation: [init][weighting?][PFE]<sub>[norm]</sub><sup>[size]</sup>, where [init] is either 'g', 'h', or 's', denoting initialization based on GMM, hierarchical clustering or WSC (the new scheme); [weighting?] is either 'w' or 'o', denoting whether residual-based channel weighting is turned on or not; [size] is the width of neighborhood window (default value is 11); and [norm] is either '1' or 'p', '1' for the  $L_{1,1}$ -regularized objective and 'p' for the  $L_{1,p}$ -regularized ( $p \neq 1$ ) objective. For example, goPFE<sub>1</sub>, the same version as in [21], meaning PFE is computed using the  $L_{1,1}$ -regularized objective in (7) and GMM based initialization without channel weighting. And swPFE<sub>p</sub> means PFE is computed using the  $L_{1,p}$ -regularized objective in (3), residual-based channel weighting and the WSC initialization.

## 5.1 Results and Comparison

**Segmentation Using PFE vs Other Existing Methods** In the framework of clustering-based segmentation, methods incorporating our piecewise flat embedding achieve significantly better performance than those adopting Normalized Cuts including spectral clustering and weighted spectral

TABLE 4

Segmentation performance on the SBD dataset. Our method performs favorably against its LE counterpart and previous methods.

method	$F_b$		$F_{op}$		Covering		PRI		VI	
	ODS	OIS	ODS	OIS	ODS	OIS	ODS	OIS	ODS	OIS
gPb-owt-ucm [10]	0.534	0.574	0.279	0.321	0.583	0.643	0.862	0.893	1.877	1.617
ISCRA [36]	0.539	0.582	0.298	0.340	0.616	0.676	0.871	0.901	1.725	1.493
MCG [2]	0.543	0.585	0.300	0.345	0.598	0.663	0.870	0.897	1.756	1.501
LEP [37]	0.550	0.597	0.331	0.374	0.620	0.689	0.874	0.903	1.629	1.399
DB [59]	0.631	0.667	0.329	0.375	0.667	0.724	0.890	0.920	1.532	1.314
LE+DB	0.633	0.670	0.336	0.379	0.663	0.720	0.889	0.918	1.510	1.302
swPFE <sub>0.8</sub> +DB	0.634	0.669	0.369	0.407	0.681	0.734	0.892	0.922	1.403	1.229
COB [62]	<b>0.666</b>	<b>0.693</b>	0.366	0.416	0.721	0.766	0.910	0.934	1.324	1.164
LE+COB	0.663	0.689	0.371	0.417	0.722	0.764	0.911	0.933	1.308	1.168
swPFE <sub>0.8</sub> +COB	0.663	0.690	<b>0.380</b>	<b>0.432</b>	<b>0.728</b>	<b>0.772</b>	<b>0.911</b>	<b>0.935</b>	<b>1.292</b>	<b>1.131</b>

TABLE 5

Segmentation performance on the MSRC dataset. Our method performs favorably against its LE counterpart and previous methods.

method	$F_b$		$F_{op}$		Covering		PRI		VI	
	ODS	OIS	ODS	OIS	ODS	OIS	ODS	OIS	ODS	OIS
gPb-owt-ucm [10]	0.468	0.524	0.458	0.525	0.651	0.743	0.779	0.845	1.274	0.980
ISCRA [36]	0.463	0.530	0.486	0.524	0.667	0.746	0.767	0.845	1.166	1.024
MCG [2]	0.479	0.537	0.467	0.536	0.667	0.745	0.784	0.848	1.205	0.961
LEP [37]	0.499	0.553	0.497	0.538	0.677	0.741	0.792	0.843	1.190	1.051
DB [59]	0.570	0.623	0.522	0.608	0.733	0.808	0.825	0.888	1.061	0.806
LE+DB	0.586	0.630	0.536	0.619	0.734	0.807	0.827	0.887	1.012	0.793
swPFE <sub>0.8</sub> +DB	0.587	0.632	0.559	0.634	0.748	0.816	0.835	0.891	0.970	0.761
COB [62]	0.597	0.634	0.559	0.635	0.764	0.823	0.848	0.895	0.966	0.760
LE+COB	0.591	0.630	0.559	0.621	0.757	0.814	0.845	0.888	0.980	0.783
swPFE <sub>0.8</sub> +COB	<b>0.598</b>	<b>0.636</b>	<b>0.572</b>	<b>0.642</b>	<b>0.767</b>	<b>0.824</b>	<b>0.850</b>	<b>0.893</b>	<b>0.953</b>	<b>0.751</b>

clustering, as shown in Tables 1 and 2. In particular, variant of our embedding, swPFE<sub>0.8</sub>, achieves 0.247 on  $F_{op}$  (fixed scheme), which is 54.4% higher than the corresponding method using Laplacian eigenmaps. In the context of hierarchical image segmentation, as our embedding is not a standalone segmentation algorithm, we demonstrate that incorporating our embedding makes existing hierarchical algorithms achieve clearly better performance. As shown in Table 3, once PFE is integrated into gPb-owt-ucm, the resulting algorithm, 'swPFE<sub>0.8</sub>+mPb', exhibits better performance under all considered metrics. Its  $F_{op}$  (OIS) is increased from 0.385 to 0.411, and VI (ODS) is improved from 1.690 to 1.565. Likewise, 'swPFE<sub>0.8</sub>+MCG' delivers better performance than the original MCG under all metrics. After further replacing the local contours in gPb-owt-ucm with those computed using Deep Boundaries [59], the resulting 'swPFE<sub>0.8</sub>+DB' delivers substantially better performances than its LE counterpart ('LE+DB'), and achieves state-of-the-art performance on BSDS500 in the contour-driven hierarchical segmentation framework. Note that, as we mentioned earlier, our objective function bears some resemblance with the energy function of total variation, which is typically applied to image denoising and restoration. We have attempted to make use of it in image segmentation by directly extracting global contours from its output. However, the result is not comparable to those of recent methods reported in Table 3. Consistently favorable results are delivered by our PFE-based method on the SBD dataset (Table 4) and the MSRC dataset (Table 6).

In table 4, performances of MS-NCut [63] and Mean

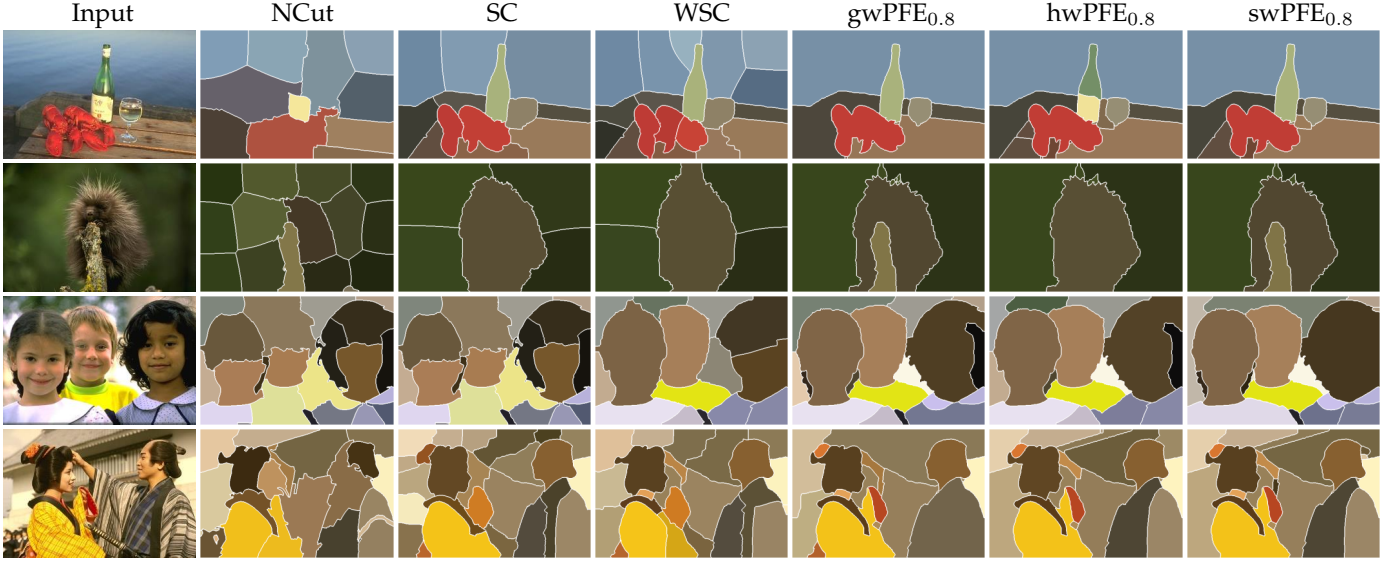


Fig. 10. Comparison of clustering based segmentation methods. Normalized Cut is based on the original local boundary cues; the other methods adopt local boundary cues from DB [59]. All the previous methods tend to produce segments that break a semantically coherent region. The results of three different initialization options of our method are shown.

TABLE 6

Segmentation performance on PASCAL Context dataset. Our method performs favorably against its LE counterpart and other methods.

method	$F_b$		$F_{op}$		Covering		PRI		VI	
	ODS	OIS	ODS	OIS	ODS	OIS	ODS	OIS	ODS	OIS
MCG [2]	0.577	0.634	0.356	0.419	0.577	0.668	0.798	0.854	1.680	1.332
DB [59]	0.680	0.731	0.413	0.489	0.658	0.748	0.840	0.896	1.421	1.112
LE+DB	0.688	0.736	0.416	0.491	0.663	0.744	0.840	0.893	1.395	1.114
swPFE <sub>0.8</sub> +DB	0.691	0.741	0.437	0.511	0.669	0.753	0.841	0.898	1.327	1.060
COB [37]	0.755	0.789	0.490	0.566	0.739	0.803	0.878	0.919	1.150	0.916
LE+COB	0.602	0.655	0.350	0.417	0.588	0.675	0.806	0.859	1.693	1.332
swPFE <sub>0.8</sub> +COB	<b>0.757</b>	<b>0.791</b>	<b>0.503</b>	<b>0.578</b>	<b>0.743</b>	<b>0.806</b>	<b>0.880</b>	<b>0.920</b>	<b>1.129</b>	<b>0.894</b>

TABLE 7

Experiment with different initialization and weighting options in the contour-driven hierarchical segmentation task on BSDS500.

method	$F_b$		$F_{op}$		Covering		PRI		VI	
	ODS	OIS	ODS	OIS	ODS	OIS	ODS	OIS	ODS	OIS
goPFE <sub>0.8</sub> + DB	0.809	0.830	0.435	0.491	0.661	0.713	0.857	0.885	1.393	1.216
hoPFE <sub>0.8</sub> + DB	0.808	0.831	0.437	0.494	0.662	0.713	0.856	0.885	1.387	1.210
soPFE <sub>0.8</sub> + DB	0.808	0.831	0.438	0.494	0.663	0.713	0.856	0.885	1.380	1.204
gwPFE <sub>0.8</sub> + DB	0.808	0.831	0.440	0.496	0.665	0.712	0.857	0.882	1.330	1.191
hwPFE <sub>0.8</sub> + DB	0.809	0.831	0.465	0.514	0.675	0.722	0.860	0.888	1.302	1.152
swPFE <sub>0.5</sub> + DB	0.808	0.830	0.450	0.504	0.666	0.715	0.854	0.883	1.316	1.169
swPFE <sub>0.8</sub> + DB	0.809	0.832	0.463	0.514	0.680	0.722	0.860	0.887	1.293	1.145
swPFE <sub>1</sub> + DB	0.809	0.832	0.462	0.512	0.672	0.720	0.859	0.886	1.315	1.156

Shift [25] are taken from [10]. The result of Hoiem [64] is from [36]. Other methods are evaluated through the SEISM toolbox [60]. For COB [62], we use the precomputed result provided by SEISM.

In addition to region-oriented measures, boundary-oriented measures are also widely used to evaluate the performance of image segmentation. Since our embedding focuses on flattening regions and we still use existing local contour detection algorithms in contour-driven segmentation, our piecewise flat embedding tends to substantially improve region-oriented segmentation measures while achiev-

ing equivalent or slightly better results under the boundary-oriented measure ( $F_b$ ). Precision-recall curves of various segmentation algorithms on the BSDS500, SBD, and MSRC dataset for the boundary and “objects and parts” measure are shown in Figure 11.

**Initialization Schemes** Table 7 shows performance perturbation of different initialization schemes, and of weighted vs. original PFE schemes. The experiments are conducted on the BSDS500 dataset. The initialization schemes are GMM, hierarchical segmentation, and WSC that we described in section 4. In the original PFE scheme, i.e. without the residual-based channel weighting, the three initialization schemes make little differences (the top three rows). With the weighting scheme, GMM is noticeably worse, and WSC is slightly better than hierarchical-based initialization. For example,  $F_{op}$  (ODS) measure of ‘gwPFE<sub>0.8</sub>+DB’ is 0.44 while the other two are both over 0.46; the VI (OIS) measure of ‘gwPFE<sub>0.8</sub>+DB’ is 1.191, while ‘hwPFE<sub>0.8</sub>+DB’ is 1.152 and ‘swPFE<sub>0.8</sub>+DB’ is 1.145. Experimental result on the other datasets exhibits similar behavior.

**Original PFE vs Weighted PFE** The residual-based channel weighting makes a clear difference in all three initialization schemes. For example, if we compare  $F_{op}$  (ODS) measure of ‘swPFE<sub>0.8</sub>+DB’ against ‘soPFE<sub>0.8</sub>+DB’, the former is 0.559 while the latter is 0.522. Because the three initialization schemes without weighting perform almost equally, and the WSC initialization with the weighting performs overall the best, it means the weighting scheme is most effective with the WSC initialization. For example, on the  $F_{op}$  (ODS) measure, the performance gain with weighting on the GMM, hierarchical and WSC initializations are 4%, 5%, and 7%, respectively. Besides, further experiments show that the weighting scheme has less effect in the clustering-based segmentation framework.

A gallery of segmentation results from various algorithms and comparisons can be found in Figures 10, 13 and 14.

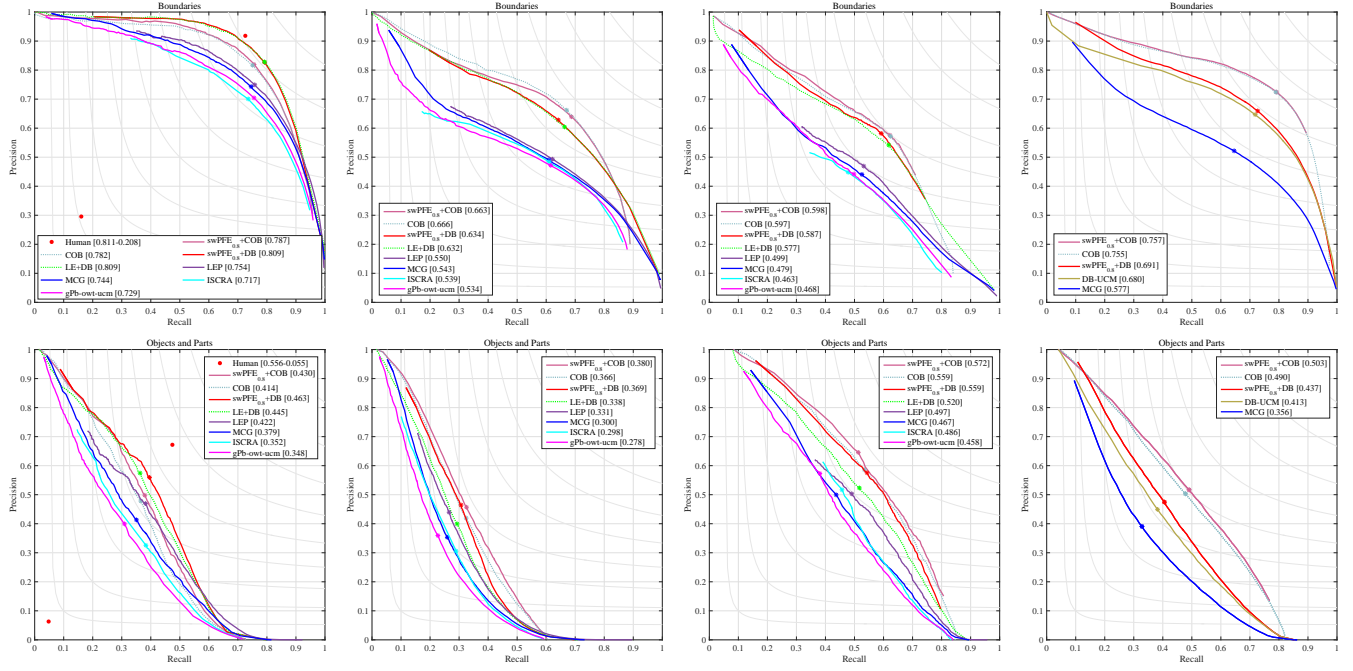


Fig. 11. Top: Precision-recall curves for the boundary measure  $F_b$ ; Bottom: Precision-recall curves for the objects and parts measure  $F_{op}$ . From left to right are results on the BSDS500, SBD, MSRC and PASCAL Context dataset, respectively. Our method (swPFE<sub>0.8</sub> + DB) consistently outperforms previous methods.

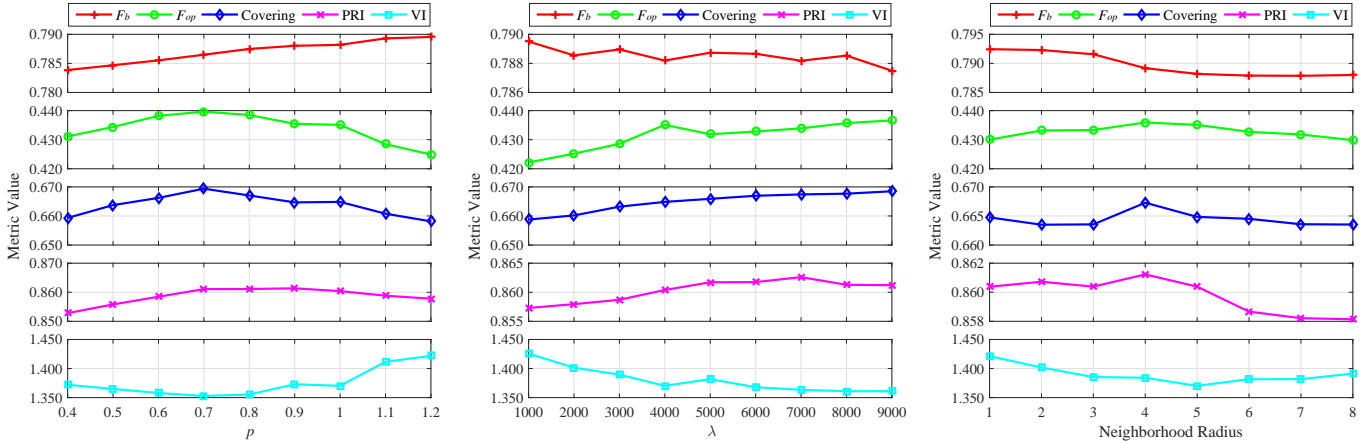


Fig. 12. Ablation analysis of parameters ( $p$ ,  $\lambda$ , and neighborhood size) on final segmentation performance (ODS values of five measures). In each experiment, all parameters except for the analyzed one are fixed to the default setting. Experiments are conducted on the BSDS500 dataset in the contour-driven hierarchical segmentation framework.

## 5.2 Parameter Choice

In addition to the categorical parameters such as initialization and channel weighting option, let's further investigate the effects of a few important continuous parameters on the final segmentation performance. These parameters include  $p$ ,  $\lambda$ , and neighborhood size. We use the contour-driven hierarchical segmentation framework for this evaluation, and take the ODS value of all five performance metrics for this evaluation. The results are plotted in Figure 12.

- $p$  controls the sparsity of the embedding. Smaller  $p$  improves the sparsity. However a sparser embedding does not always gives rise to better segmentation performance. In our evaluation, the best result is achieved around  $p = 0.7$  under all measures except for  $F_b$ , which improves as  $p$  increases.
- As shown in step (a.1) (Appendix A),  $\lambda$  is the weight of

the  $L_{1,1}$ -regularized energy term. It balances between the sparsity of the embedding and the orthogonality among the embedding channels. The five performance metrics do not change consistently as  $\lambda$  varies. It produces the best result with respect to PRI when  $\lambda$  is around 7000. However,  $F_{op}$ , Covering and VI become better overall as  $\lambda$  increases, and  $F_b$  remains stable within our testing range with the maximum variation less than 0.003.

- **Neighborhood Size** A larger neighborhood allows direct interaction among pixels further apart, but decreases the sparsity of boundary-crossing connections. The best performance on BSDS500 under four measures other than  $F_b$  is achieved when the neighborhood radius is around 4 (translates to a  $9 \times 9$  neighborhood size), while  $F_b$  benefits from smaller neighborhood radius size (2 to 3).

## 6 CONCLUSIONS

We have presented a new nonlinear embedding called piecewise flat embedding for image segmentation. We adopt an  $L_{1,p}$ -regularized ( $0 < p \leq 1$ ) energy term in the objective function to promote sparse solutions. To solve the  $L_{1,1}$ -regularized objective function, a two-stage numerical algorithm is first developed by nesting two existing solvers. Then we generalize this numerical algorithm through iterative reweighting to solve the  $L_{1,p}$ -regularized problem. Experiments on BSDS500, MSRC and SBD indicate that segmentation methods incorporating our embedding can achieve significantly improved results.

## ACKNOWLEDGMENTS

This work is supported in part by Hong Kong Research Grants Council under General Research Funds (HKU719313) and by The National Natural Science Foundation under Young Researcher Grant (No. 61602406).

## REFERENCES

- [1] D. Marr, "A computational investigation into the human representation and processing of visual information," *Vision*, pp. 125–126, 1982.
- [2] J. Pont-Tuset, P. Arbelaez, J. T. Barron, F. Marques, and J. Malik, "Multiscale combinatorial grouping for image segmentation and object proposal generation," *IEEE transactions on pattern analysis and machine intelligence*, vol. 39, no. 1, pp. 128–140, 2017.
- [3] J. Fan, D. K. Yau, A. K. Elmagarmid, and W. G. Aref, "Automatic image segmentation by integrating color-edge extraction and seeded region growing," *IEEE transactions on image processing*, vol. 10, no. 10, pp. 1454–1466, 2001.
- [4] T. Chen, M.-M. Cheng, P. Tan, A. Shamir, and S.-M. Hu, "Sketch2photo: Internet image montage," *ACM Transactions on Graphics (TOG)*, vol. 28, no. 5, p. 124, 2009.
- [5] J. Kim, D. Han, Y.-W. Tai, and J. Kim, "Salient region detection via high-dimensional color transform and local spatial support," *IEEE transactions on image processing*, vol. 25, no. 1, pp. 9–23, 2016.
- [6] S. Bi, X. Han, and Y. Yu, "An l1 image transform for edge-preserving smoothing and scene-level intrinsic decomposition," *ACM Transactions on Graphics (TOG)*, vol. 34, no. 4, p. 78, 2015.
- [7] E. H. Land and J. J. McCann, "Lightness and retinex theory," *Journal of the Optical Society of America*, vol. 61, no. 1, pp. 1–11, Jan 1971. [Online]. Available: <http://www.osapublishing.org/abstract.cfm?URI=josa-61-1-1>
- [8] D. R. Martin, C. C. Fowlkes, and J. Malik, "Learning to detect natural image boundaries using local brightness, color, and texture cues," *Pattern Analysis and Machine Intelligence, IEEE Transactions on*, vol. 26, no. 5, pp. 530–549, 2004.
- [9] J. Malik, S. Belongie, T. Leung, and J. Shi, "Contour and texture analysis for image segmentation," *International journal of computer vision*, vol. 43, no. 1, pp. 7–27, 2001.
- [10] P. Arbelaez, M. Maire, C. Fowlkes, and J. Malik, "Contour detection and hierarchical image segmentation," *Pattern Analysis and Machine Intelligence, IEEE Transactions on*, vol. 33, no. 5, pp. 898–916, 2011.
- [11] J. Shi and J. Malik, "Normalized cuts and image segmentation," *Pattern Analysis and Machine Intelligence, IEEE Transactions on*, vol. 22, no. 8, pp. 888–905, 2000.
- [12] D. L. Donoho and P. B. Stark, "Uncertainty principles and signal recovery," *SIAM Journal on Applied Mathematics*, vol. 49, no. 3, pp. 906–931, 1989.
- [13] D. L. Donoho and B. F. Logan, "Signal recovery and the large sieve," *SIAM Journal on Applied Mathematics*, vol. 52, no. 2, pp. 577–591, 1992.
- [14] T. Goldstein and S. Osher, "The split bregman method for l1-regularized problems," *SIAM Journal on Imaging Sciences*, vol. 2, no. 2, pp. 323–343, 2009.
- [15] R. Lai and S. Osher, "A splitting method for orthogonality constrained problems," *Journal of Scientific Computing*, vol. 58, no. 2, pp. 431–449, 2014.
- [16] P. Ochs, A. Dosovitskiy, T. Brox, and T. Pock, "On iteratively reweighted algorithms for nonsmooth nonconvex optimization in computer vision," *SIAM Journal on Imaging Sciences*, vol. 8, no. 1, pp. 331–372, 2015.
- [17] S. Gould, R. Fulton, and D. Koller, "Decomposing a scene into geometric and semantically consistent regions," in *Computer Vision, 2009 IEEE 12th International Conference on*. IEEE, 2009, pp. 1–8.
- [18] T. Malisiewicz and A. A. Efros, "Improving spatial support for objects via multiple segmentations," in *Proceedings of the British Machine Vision Conference*. BMVA Press, 2007, pp. 55.1–55.10, doi:10.5244/C.21.55.
- [19] J. Shotton, J. Winn, C. Rother, and A. Criminisi, "Textonboost: Joint appearance, shape and context modeling for multi-class object recognition and segmentation," in *European conference on computer vision*. Springer, 2006, pp. 1–15.
- [20] R. Mottaghi, X. Chen, X. Liu, N.-G. Cho, S.-W. Lee, S. Fidler, R. Urtasun, and A. Yuille, "The role of context for object detection and semantic segmentation in the wild," in *Proceedings of the IEEE Conference on Computer Vision and Pattern Recognition*, 2014, pp. 891–898.
- [21] Y. Yu, C. Fang, and Z. Liao, "Piecewise flat embedding for image segmentation," in *Proceedings of the IEEE International Conference on Computer Vision*, 2015, pp. 1368–1376.
- [22] Y. Chen, T. A. Davis, W. W. Hager, and S. Rajamanickam, "Algorithm 887: Cholmod, supernodal sparse cholesky factorization and update/downdate," *ACM Transactions on Mathematical Software (TOMS)*, vol. 35, no. 3, p. 22, 2008.
- [23] J. MacQueen et al., "Some methods for classification and analysis of multivariate observations," in *Proceedings of the fifth Berkeley symposium on mathematical statistics and probability*, vol. 1, no. 14. Oakland, CA, USA., 1967, pp. 281–297.
- [24] G. McLachlan and D. Peel, *Finite mixture models*. John Wiley & Sons, 2004.
- [25] D. Comaniciu and P. Meer, "Mean shift: A robust approach toward feature space analysis," *Pattern Analysis and Machine Intelligence, IEEE Transactions on*, vol. 24, no. 5, pp. 603–619, 2002.
- [26] D. Greig, B. Porteous, and A. H. Seheult, "Exact maximum a posteriori estimation for binary images," *Journal of the Royal Statistical Society. Series B (Methodological)*, pp. 271–279, 1989.
- [27] Y. Boykov, O. Veksler, and R. Zabih, "Fast approximate energy minimization via graph cuts," *Pattern Analysis and Machine Intelligence, IEEE Transactions on*, vol. 23, no. 11, pp. 1222–1239, 2001.
- [28] V. Kolmogorov and R. Zabih, "What energy functions can be minimized via graph cuts?" *Pattern Analysis and Machine Intelligence, IEEE Transactions on*, vol. 26, no. 2, pp. 147–159, 2004.
- [29] P. F. Felzenszwalb and D. P. Huttenlocher, "Efficient graph-based image segmentation," *International Journal of Computer Vision*, vol. 59, no. 2, pp. 167–181, 2004.
- [30] M. Maire, P. Arbelaez, C. Fowlkes, and J. Malik, "Using contours to detect and localize junctions in natural images," in *2008 IEEE Conference on Computer Vision and Pattern Recognition*, June 2008, pp. 1–8.
- [31] L. Najman and M. Schmitt, "Geodesic saliency of watershed contours and hierarchical segmentation," *Pattern Analysis and Machine Intelligence, IEEE Transactions on*, vol. 18, no. 12, pp. 1163–1173, 1996.
- [32] P. Arbelaez, M. Maire, C. Fowlkes, and J. Malik, "From contours to regions: An empirical evaluation," in *2009 IEEE Conference on Computer Vision and Pattern Recognition*, June 2009, pp. 2294–2301.
- [33] R. Xiaofeng and L. Bo, "Discriminatively trained sparse code gradients for contour detection," in *Advances in neural information processing systems*, 2012, pp. 584–592.
- [34] P. Dollár and C. L. Zitnick, "Fast edge detection using structured forests," *Pattern Analysis and Machine Intelligence, IEEE Transactions on*, vol. 37, no. 8, pp. 1558–1570, 2015.
- [35] S. Xie and Z. Tu, "Holistically-nested edge detection," *International Journal of Computer Vision*, vol. 125, no. 1, pp. 3–18, Dec 2017. [Online]. Available: <https://doi.org/10.1007/s11263-017-1004-z>
- [36] Z. Ren and G. Shakhnarovich, "Image segmentation by cascaded region agglomeration," in *Proceedings of the IEEE Conference on Computer Vision and Pattern Recognition*, 2013, pp. 2011–2018.
- [37] Q. Zhao, "Segmenting natural images with the least effort as humans," in *Proceedings of the British Machine Vision Conference (BMVC)*, M. W. J. Xianghua Xie and G. K. L. Tam, Eds. BMVA Press, September 2015, pp. 110.1–110.12. [Online]. Available: <https://dx.doi.org/10.5244/C.29.110>



- [38] S. Osher and J. Sethian, "Fronts propagation with curvature dependent speed: Algorithms based on hamilton-jacobi formulations," *Journal of Computational Physics*, 1988.
- [39] T. F. Chan and L. A. Vese, "Active contours without edges," *IEEE Transactions on image processing*, vol. 10, no. 2, pp. 266–277, 2001.
- [40] S. T. Roweis and L. K. Saul, "Nonlinear dimensionality reduction by locally linear embedding," *Science*, vol. 290, no. 5500, pp. 2323–2326, 2000.
- [41] M. Belkin and P. Niyogi, "Laplacian eigenmaps for dimensionality reduction and data representation," *Neural computation*, vol. 15, no. 6, pp. 1373–1396, 2003.
- [42] L. Van der Maaten and G. Hinton, "Visualizing data using t-sne," *Journal of Machine Learning Research*, vol. 9, no. 2579–2605, p. 85, 2008.
- [43] L. Van Der Maaten, "Accelerating t-sne using tree-based algorithms," *The Journal of Machine Learning Research*, vol. 15, no. 1, pp. 3221–3245, 2014.
- [44] G. E. Hinton and S. T. Roweis, "Stochastic neighbor embedding," in *Advances in neural information processing systems*, 2002, pp. 833–840.
- [45] D. Cai, X. He, J. Han, and T. S. Huang, "Graph regularized nonnegative matrix factorization for data representation," *Pattern Analysis and Machine Intelligence, IEEE Transactions on*, vol. 33, no. 8, pp. 1548–1560, 2011.
- [46] J. B. Tenenbaum, V. De Silva, and J. C. Langford, "A global geometric framework for nonlinear dimensionality reduction," *science*, vol. 290, no. 5500, pp. 2319–2323, 2000.
- [47] B. Shaw and T. Jebara, "Structure preserving embedding," in *Proceedings of the 26th Annual International Conference on Machine Learning*. ACM, 2009, pp. 937–944.
- [48] E. Elhamifar and R. Vidal, "Sparse manifold clustering and embedding," in *Advances in neural information processing systems*, 2011, pp. 55–63.
- [49] H. V. Nguyen, V. M. Patel, N. M. Nasrabadi, and R. Chellappa, "Sparse embedding: A framework for sparsity promoting dimensionality reduction," in *Computer Vision–ECCV 2012*. Springer, 2012, pp. 414–427.
- [50] E. Elhamifar and R. Vidal, "Sparse subspace clustering: Algorithm, theory, and applications," *IEEE transactions on pattern analysis and machine intelligence*, vol. 35, no. 11, pp. 2765–2781, 2013.
- [51] F. Tian, B. Gao, Q. Cui, E. Chen, and T.-Y. Liu, "Learning deep representations for graph clustering," in *AAAI*, 2014, pp. 1293–1299.
- [52] S. Chang, W. Han, J. Tang, G.-J. Qi, C. C. Aggarwal, and T. S. Huang, "Heterogeneous network embedding via deep architectures," in *Proceedings of the 21th ACM SIGKDD International Conference on Knowledge Discovery and Data Mining*. ACM, 2015, pp. 119–128.
- [53] L. I. Rudin, S. Osher, and E. Fatemi, "Nonlinear total variation based noise removal algorithms," *Physica D: Nonlinear Phenomena*, vol. 60, no. 1, pp. 259–268, 1992.
- [54] L. M. Bregman, "The relaxation method of finding the common point of convex sets and its application to the solution of problems in convex programming," *USSR computational mathematics and mathematical physics*, vol. 7, no. 3, pp. 200–217, 1967.
- [55] D. Geman and G. Reynolds, "Constrained restoration and the recovery of discontinuities," *IEEE Transactions on pattern analysis and machine intelligence*, vol. 14, no. 3, pp. 367–383, 1992.
- [56] I. Daubechies, R. DeVore, M. Fornasier, and C. S. Güntürk, "Iteratively reweighted least squares minimization for sparse recovery," *Communications on Pure and Applied Mathematics*, vol. 63, no. 1, pp. 1–38, 2010.
- [57] E. J. Candes, M. B. Wakin, and S. P. Boyd, "Enhancing sparsity by reweighted  $\ell_1$  minimization," *Journal of Fourier analysis and applications*, vol. 14, no. 5–6, pp. 877–905, 2008.
- [58] S. Belongie and J. Malik, *Finding boundaries in natural images: A new method using point descriptors and area completion*. Berlin, Heidelberg: Springer Berlin Heidelberg, 1998, pp. 751–766.
- [59] I. Kokkinos, "Pushing the boundaries of boundary detection using deep learning," *arXiv preprint arXiv:1511.07386*, 2015.
- [60] J. Pont-Tuset and F. Marques, "Supervised evaluation of image segmentation and object proposal techniques," *IEEE Transactions on Pattern Analysis and Machine Intelligence*, vol. 38, no. 7, pp. 1465–1478, 2016.
- [61] M. Everingham, L. Van Gool, C. K. Williams, J. Winn, and A. Zisserman, "The pascal visual object classes (voc) challenge," *International journal of computer vision*, vol. 88, no. 2, pp. 303–338, 2010.
- [62] K. Maninis, J. Pont-Tuset, P. Arbeláez, and L. V. Gool, "Convolutional oriented boundaries: From image segmentation to high-level tasks," *IEEE Transactions on Pattern Analysis and Machine Intelligence (TPAMI)*, 2017.
- [63] T. Cour, F. Benezit, and J. Shi, "Spectral segmentation with multi-scale graph decomposition," in *Computer Vision and Pattern Recognition, 2005. CVPR 2005. IEEE Computer Society Conference on*, vol. 2. IEEE, 2005, pp. 1124–1131.
- [64] D. Hoiem, A. A. Efros, and M. Hebert, "Recovering occlusion boundaries from an image," *International Journal of Computer Vision*, vol. 91, no. 3, pp. 328–346, 2011.

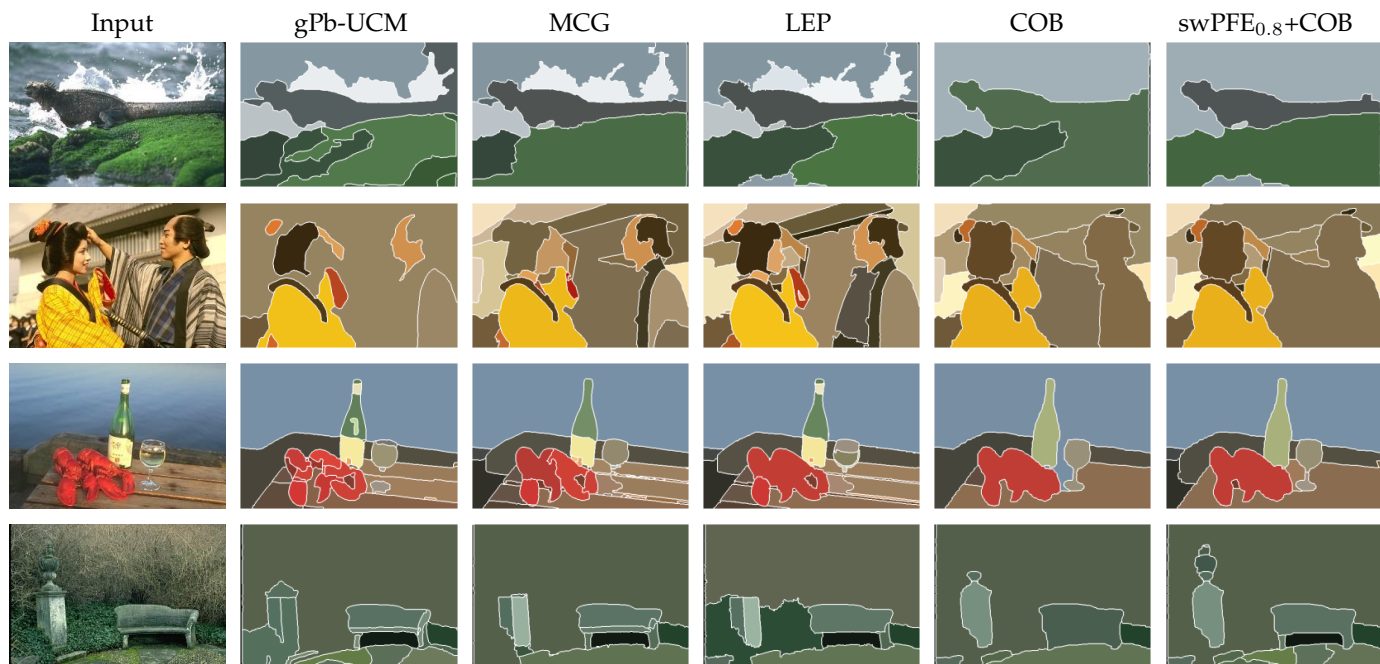


Fig. 13. Comparison of contour-driven hierarchical segmentation methods on BSDS500. 'swPFE<sub>0.8</sub>+COB' denotes the contour-driven segmentation algorithm that integrates swPFE<sub>0.8</sub> while utilizing local boundary information from COB.

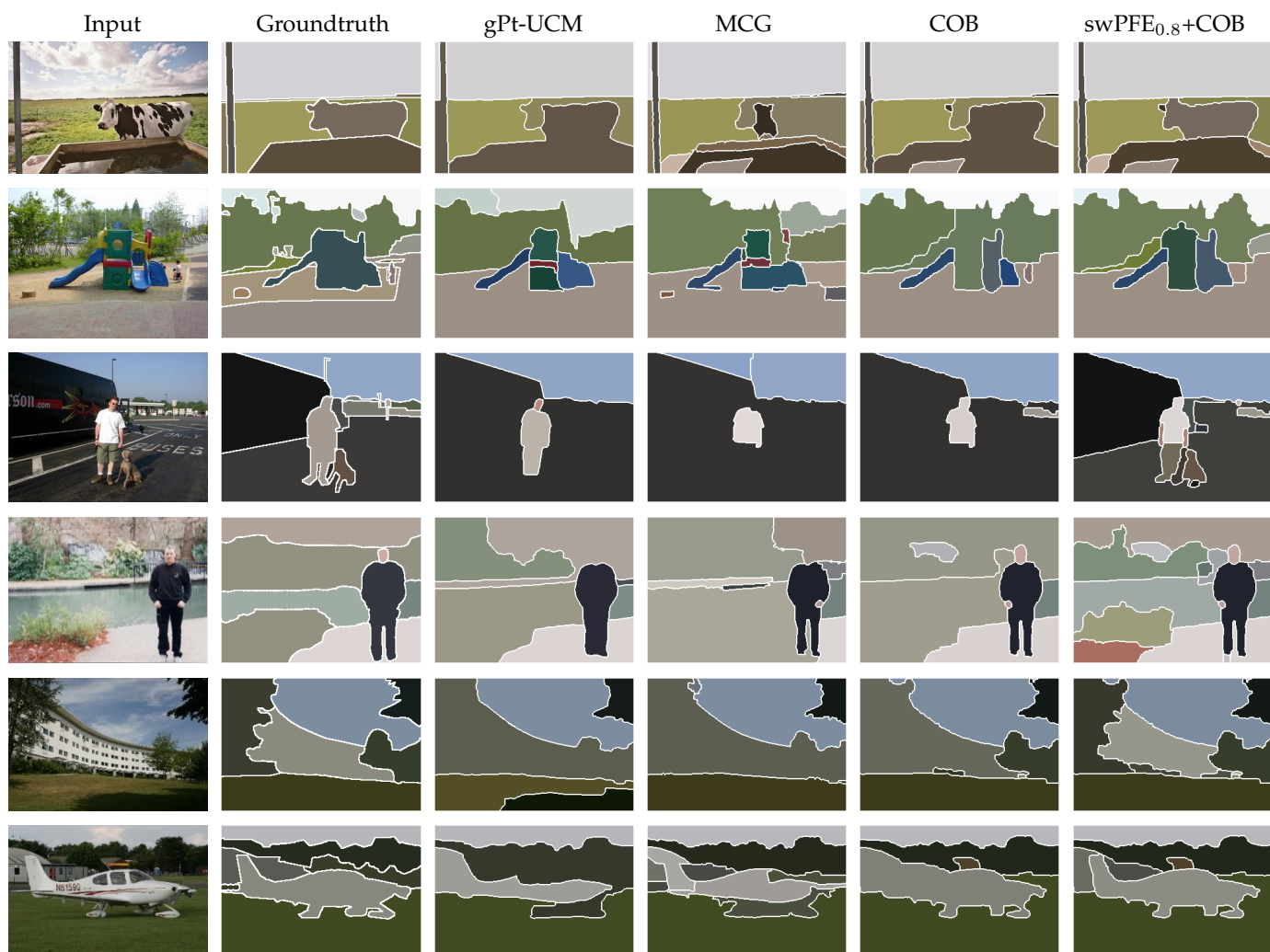


Fig. 14. Comparison of contour-driven hierarchical segmentation methods on SBD and MSRC. Top 3 images are selected from SBD, and other images are from MSRC.

## APPENDIX A

### $L_{1,1}$ -REGULARIZED MINIMIZATION

According to the Split Bregman algorithm [14], the  $L_{1,1}$ -regularized problem in step (a) of equation 8 can be solved by iterating the following steps:

$$(a.1) \quad \mathbf{Y}^{(k,l+1)} = \arg \min_{\mathbf{Y}} \frac{\lambda}{2} \|\mathbf{M}\mathbf{Y} + \mathbf{E}^l - \mathbf{C}^l\|_{2,2}^2 + \frac{r}{2} \|\mathbf{D}^{1/2}\mathbf{Y} - \mathbf{F}^{(k)}\|_{2,2}^2;$$

$$(a.2) \quad \mathbf{C}^{l+1} = \arg \min_{\mathbf{C}} \|\mathbf{C}\|_{1,1} + \frac{\lambda}{2} \|\mathbf{C} - \mathbf{M}\mathbf{Y}^{(k,l+1)} - \mathbf{E}^l\|_{2,2}^2;$$

$$(a.3) \quad \mathbf{E}^{l+1} = \mathbf{E}^l + \mathbf{M}\mathbf{Y}^{(k,l+1)} - \mathbf{C}^{l+1}.$$

until  $\|\mathbf{Y}^{(k,l+1)} - \mathbf{Y}^{(k,l)}\| \leq \epsilon$ . Note that in the above steps,  $\mathbf{C}$  and  $\mathbf{E}$  are two auxiliary matrices,  $\mathbf{C}^0 = \mathbf{E}^0 = \mathbf{0}$ ,  $\mathbf{Y}^{(k,0)} = \mathbf{Y}^{(k)}$ ,  $\mathbf{F}^{(k)} = \mathbf{P}^{(k)} - \mathbf{B}^{(k)}$ , and  $\epsilon$  is a predefined error tolerance. The problem in (a.1) is a least-squares problem and can be easily solved through the following sparse linear system,

$$\mathbf{L}\mathbf{Y} = r\mathbf{D}^{1/2}\mathbf{F}^{(k)} + \lambda\mathbf{M}^T(\mathbf{C}^l - \mathbf{E}^l), \quad (13)$$

where  $\mathbf{L} = \lambda\mathbf{S} + r\mathbf{D}$ , and  $\mathbf{S}(= \mathbf{M}^T\mathbf{M})$  can be explicitly defined as

$$\mathbf{S} = \begin{pmatrix} \sum_{j \neq 1} W_{1j}^2 & -W_{12}^2 & \cdots & -W_{1n}^2 \\ -W_{21}^2 & \sum_{j \neq 2} W_{2j}^2 & \cdots & -W_{2n}^2 \\ \vdots & \vdots & \ddots & \vdots \\ -W_{n1}^2 & -W_{n2}^2 & \cdots & \sum_{j \neq n} W_{nj}^2 \end{pmatrix},$$

where  $W_{ij} = 0$  if there exists no connection between  $x_i$  and  $x_j$ .

Matrix  $\mathbf{L}$  has the following two important characteristics: 1)  $\mathbf{L}$  stays the same across iterations and only the right hand side of (13) evolves; 2)  $\mathbf{L}$  is sparse, symmetric and positive definite as it is a Hermitian diagonally dominant matrix with real positive diagonal entries. So  $\mathbf{L}$  only needs to be decomposed once for all iterations using a sparse matrix solver. In practice, we use Cholesky matrix decomposition to factorize matrix  $\mathbf{L}$ :  $\mathbf{L} = \mathbf{\Lambda}\mathbf{\Lambda}^T$  where  $\mathbf{\Lambda}$  is a lower triangular matrix. Thus (13) is equivalent to two triangular systems,

$$\begin{aligned} \mathbf{\Lambda}\tilde{\mathbf{Y}} &= r\mathbf{D}^{1/2}\mathbf{F}^{(k)} + \lambda\mathbf{M}^T(\mathbf{C}^l - \mathbf{E}^l), \\ \mathbf{\Lambda}^T\mathbf{Y} &= \tilde{\mathbf{Y}}. \end{aligned} \quad (14)$$

During each iteration, the extremely efficient forward and backward substitution method can be used to solve the sparse linear system in (13). This is the main reason for our choice of the Splitting Bregman algorithm in solving our  $L_{1,1}$ -regularized optimization.

In the conference version, we use the `mldivide` function in MATLAB, which performs Cholesky decomposition internally without returning the triangular matrix. Thus, we had to unnecessarily perform Cholesky decomposition in every iteration when solving (13). In this work, we perform Cholesky decomposition to factorize matrix  $\mathbf{L}$  only once and save the resulting triangular matrix. This allows us to solve two triangular systems only in every iteration, as shown in (14). This gives rise to a much faster algorithm. In a test run on 200 sample images from the BSDS500 dataset,

the average computation time of `swPFE1` drops from 233 seconds to 60 seconds.

The problem in (a.2) has a closed form solution called shrinkage operation defined as follows,

$$\mathbf{C}^{l+1} = \text{Shrink}(\mathbf{M}\mathbf{Y}^{(k,l+1)} + \mathbf{E}^l, 1/\lambda). \quad (15)$$

Suppose  $\mathbf{Z} = \text{Shrink}(\mathbf{X}, \gamma)$ . Then  $Z_{ij} = \text{sign}(X_{ij}) \max(|X_{ij}| - \gamma, 0)$ .

## APPENDIX B

### $L_{1,p}$ -REGULARIZED MINIMIZATION

Suppose  $\mathbf{M} = [\mathbf{m}_1, \dots, \mathbf{m}_t]^T$  where  $\mathbf{m}_i^T$  is the  $i$ -th row of  $\mathbf{M}$ . The problem in (11) can be rewritten as,

$$\mathbf{Y} = \arg \min_{\mathbf{Y}} \sum_{i=1}^t \|\mathbf{m}_i^T \mathbf{Y}\|_1^p + \Psi(\mathbf{Y}) \quad (16)$$

According to [16], the majorization-minimization algorithm can be applied to solve problem (11) in the form of the following iterative algorithm which makes the energy value monotonically decrease when  $0 < p < 1$ .

- ① Solve the following nonsmooth  $L_{1,1}$ -regularized problem,

$$\begin{aligned} \mathbf{Y}^{(k+1)} &= \arg \min_{\mathbf{Y}} \sum_{i=1}^t w_i^k \|\mathbf{m}_i^T \mathbf{Y}\|_1 + \Psi(\mathbf{Y}) \\ &= \arg \min_{\mathbf{Y}} \|\hat{\mathbf{M}}^{(k)} \mathbf{Y}\|_{1,1} + \Psi(\mathbf{Y}), \end{aligned} \quad (17)$$

where  $\hat{\mathbf{M}}^{(k)} = [w_1^k \mathbf{m}_1, \dots, w_t^k \mathbf{m}_t]^T$  and  $w_i^0 = 1$ .

- ② Update the coefficient  $w_i^k$ :

$$w_i^{k+1} = p \max(\|\mathbf{m}_i^T \mathbf{Y}^{(k+1)}\|_1, \varepsilon)^{p-1},$$

where  $\varepsilon$  is a constant used for avoiding an infinite value.

Again the  $L_{1,1}$ -regularized problem in (17) can be solved using the splitting Bregman iterations described in appendix A.